# Simultaneous Reconstruction of Activity and Attenuation in Time-of-Flight PET

Ahmadreza Rezaei[1], Johan Nuyts[1], Michel Defrise[2], Girish Bal[3], Christian Michel[3], Maurizio Conti[3], Charles Watson[3]

***Abstract*— In positron emission tomography (PET) and single photon emission tomography (SPECT), attenuation correction is necessary for quantitative reconstruction of the tracer distribution. Previously, several attempts have been undertaken to estimate the attenuation coefficients from emission data only. These attempts had limited success, because the problem does not have a unique solution, and severe and persistent ”cross-talk” between the estimated activity and attenuation distributions was observed. In this paper, we show that the availability of TOF-information eliminates the cross-talk problem by destroying symmetries in the associated Fisher information matrix. We propose a maximum-a-posteriori reconstruction algorithm for jointly estimating the attenuation and activity distributions from TOF-PET data. The performance of the algorithm is studied with 2D simulations, and further illustrated with phantom experiments and with a patient scan. The estimated attenuation image is robust to noise, and does not suffer from the cross-talk that was observed in non-TOF PET. However, some constraining is still mandatory, because the TOF-data determine the attenuation sinogram only up to a constant offset.**

## I. INTRODUCTION

In nuclear medicine tomographic imaging (positron emission tomography (PET) and single photon emission tomography (SPECT)), a quantitative and artifact free reconstruction of the tracer distribution can only be obtained if an accurate correction for the photon attenuation in the body of the patient is applied. The attenuation correction factors can be obtained from transmission measurements with radioactive sources, or be derived from well-aligned CT images [1]–[3]. Since both approaches have their limitations, several groups have attempted to jointly estimate the activity and attenuation images from the emission data only [4]–[12]. These attempts were based on the use of analytical consistency conditions, discrete consistency conditions and (penalized) maximum likelihood methods. Although some useful results have been obtained, the results have generally been disappointing. Nearly all studies report the so-called cross-talk problem, where localized errors in the activity image are compensated by localized errors in the attenuation image (and vice versa). This seems to be a fundamental problem. In the maximum-likelihood approach, the problem is manifested as the presence of local maxima in the likelihood function. In cases where incomplete information about the attenuation coefficients is available, these methods can be used to estimate the missing information, which is a less ill-posed problem than estimating the entire attenuation image [13]–[15].

Time-of-Flight (TOF) Positron Emission Tomography (PET) was studied in the 1980’s, but its implementation as a clinical instrument was too challenging at the time. Thanks to recent advances in electronics and in scintillation research, TOF-PET has now been introduced in commercial systems [16]–[20]. The use of TOF-information results in faster convergence of iterative reconstruction algorithms [21] and in an improved contrast-to-noise ratio [16], [22]. Moreover, recent studies have shown that in TOF-PET, the artifacts induced by attenuation correction errors are less severe than in non-TOF PET [20]. This finding indicates that TOF PET data contain information about attenuation factors, that is not present in non-TOF PET data, justifying a study of the joint estimation problem in TOF-PET.

In this paper, the simultaneous reconstruction of the activity and attenuation from TOF-PET projections is studied as a maximum-likelihood problem, building on previous work for non-TOF emission tomography [7], [14]. In the following section this algorithm, called “MLAA” is briefly described. An analysis of the Fisher information matrix gives an intuitive explanation why cross-talk is a problem in non-TOF systems, and why the use of TOF-information eliminates this problem. However, even with TOF-PET, the problem is still underdetermined: it is found that TOF-PET data determine the activity image up to a constant factor, and the emission sinogram up to a (related) constant term. In the next section, some 2D simulations experiments are described. A 2D small scale simulation experiment was done to study the features of the Fisher matrix. 2D TOF-PET simulations of a thorax phantom were done to study MLAA-reconstruction with respect to the visual quality, bias and noise as a function of the TOF resolution. The method was also applied to fully 3D TOF-PET phantom scans and a patient scan, acquired on a commercial TOF-PET system. The results of those experiments are presented in section III and discussed in section IV.

## II. THEORY AND METHODS

### A. MLAA

In TOF-PET, the expected count $\bar{y}_{it}$ for line of response (LOR) $i$ and time difference $t$ can be expressed as follows:

$$\bar{y}_{it} = \sum_{j=1}^{J} c_{ijt} \lambda_j e^{-\sum_j l_{ij}\mu_j} + s_{it} \tag{1}$$

where $\lambda_j$ and $\mu_j$ are the activity and attenuation coefficient at voxel $j$, $J$ is the total number of voxels, $c_{ijt}$ is the sensitivity of the detector at $(i,t)$ for activity in $j$ in absence of attenuation, $l_{ij}$ is the intersection length of LOR $i$ with voxel $j$, and $s_{it}$ is the expected contribution of scatter and/or randoms. Assuming that the data are Poisson distributed, the log-likelihood function can be written as

$$L(\theta, y_{it}) = \sum_{it} y_{it} \ln \bar{y}_{it} - \bar{y}_{it} \tag{2}$$

where $y_{it}$ is the measured count at $(i,t)$ and $\theta = [\lambda^T, \mu^T]^T$ is the set of $2J$ parameters that has to be estimated. Note that summation over the TOF index ($t$) yields the corresponding

---

[1] Nuclear Medicine, K.U.Leuven, B-3000 Leuven, Belgium. [2] Nuclear Medicine, Vrije Universitiet Brussel, B-1090 Brussels, Belgium. [3] Siemens Medical Solutions, MI, Knoxville, TN, USA.

[4]This research is supported by a research grant (GOA) from K.U.Leuven.

non-TOF values, which are denoted by omitting the index $t$: $\sum_t c_{ijt} = c_{ij}$, $\sum_t y_{it} = y_i$ and $\sum_t s_{it} = s_i$.

The MLAA algorithm uses an interleaved updating: in every iteration first the activity is updated keeping the attenuation coefficients constant, and then vice versa. This can be written as follows:

$$\begin{aligned}
\forall i: \quad a_i^k &= e^{-\sum_j l_{ij}\mu_j^k} && (3)\\
\forall j: \quad \lambda_j^{k+1} &= \frac{\lambda_j^k}{\sum_{it} a_i^k c_{ijt}} \sum_{it} a_i^k c_{ijt} \frac{y_{it}}{\sum_\xi a_i^k c_{i\xi t}\lambda_\xi^k + s_{it}} && (4)\\
\forall i: \quad \psi_i^k &= a_i^k \sum_{jt} c_{ijt}\lambda_j^{k+1} && (5)\\
\forall j: \quad \mu_j^{k+1} &= \mu_j^k + \frac{\sum_i l_{ij}\dfrac{\psi_i^k}{\psi_i^k + s_i}(\psi_i^k + s_i - y_i)}{\sum_i l_{ij}\dfrac{(\psi_i^k)^2}{\psi_i^k + s_i}\sum_\xi l_{i\xi}} && (6)
\end{aligned}$$

where the superscript $k$ denotes the iteration number. The non-TOF sinogram $a^k$ represents the attenuation computed from the current estimate $\mu^k$, and the non-TOF sinogram elements $\psi_i^k$ represent the expected TOF-integrated count for LOR $i$, but without the additive contribution $s_i$. Expression (4) is a standard MLEM iteration [23], which makes explicit use of the TOF-PET data. Expression (6) is the MLTR update [24], [25], which only uses the TOF-integrated data. Note that the sinogram with elements $\sum_{jt} c_{ijt}\lambda_j^{k+1}$ plays the role of the blank scan, while the TOF integrated data $y_i$ are treated as the transmission scan.

Both MLEM and MLTR can be accelerated with ordered subsets. Furthermore, because the TOF information improves convergence of MLEM but not that of MLTR, we typically cycle through the subsets faster for the MLTR updates (using the same subsets definition for both). Thus, for every MLEM update $N \geq 1$ MLTR updates are done, and when all projections have contributed once to the activity updates, they have contributed $N$ times to the attenuation updates. This decreases the processing time considerably, also because the MLTR updates only involves non-TOF projections and backprojections. Unless otherwise stated, $N = 5$.

### *B. The curvature of the likelihood*

We analyze the curvature of the likelihood at its maximum for both TOF and non-TOF systems to get more insight in the simultaneous activity and attenuation estimation problem. We ignore the non-negativity constraint in our analysis, assume the likelihood has been maximized and then look for a small change $\Delta\theta$ that does not change the gradient of the likelihood. If such a $\Delta\theta$ can be found, then both $\theta$ and $\theta + \Delta\theta$ maximize the likelihood, implying that the problem is under-determined. For small $\Delta\theta$, the induced change of the gradient of the likelihood (which we set to zero) equals

$$\sum_k \frac{\partial^2 L}{\partial\theta_j \partial\theta_k}\Delta\theta_k = 0, \quad j = 0, ..., 2J \tag{7}$$

This can be rewritten using the Fisher information matrix (FIM) [26], [27] which is defined as minus the expectation of the second derivatives of the likelihood with respect to the parameter space:

$$F\Delta\theta = 0 \tag{8}$$

where, $F$ is the $2J \times 2J$ FIM and $\Delta\theta$ is the $2J \times 1$ matrix representing the change in the parameter space.

Replacing $\theta$ with $[\lambda^T, \theta^T]^T$, the Fisher information matrix can be rewritten in a quadrant form as follows

$$\begin{aligned}
F &= -E[\frac{\partial^2 L}{\partial\theta\partial\theta}]\\
&= \begin{pmatrix} -E[\frac{\partial^2 L}{\partial\lambda\partial\lambda}] & -E[\frac{\partial^2 L}{\partial\lambda\partial\mu}] \\ -E[\frac{\partial^2 L}{\partial\mu\partial\lambda}] & -E[\frac{\partial^2 L}{\partial\mu\partial\mu}] \end{pmatrix} = \begin{pmatrix} F_{\lambda\lambda} & F_{\lambda\mu} \\ F_{\lambda\mu}^T & F_{\mu\mu} \end{pmatrix} && (9)
\end{aligned}$$

where for all $j, k = 1, \ldots, J$ combinations,

$$\begin{aligned}
-E[\frac{\partial^2 L}{\partial\lambda_j\partial\lambda_k}] &= \sum_{i,t} \frac{c_{ijt}c_{ikt}}{\bar{y}_{it}} e^{-2\sum_\xi l_{i\xi}\mu_\xi} && (10)\\
-E[\frac{\partial^2 L}{\partial\mu_j\partial\mu_k}] &= \sum_{i,t} l_{ij}\bar{y}_{it}l_{ik} = \sum_i l_{ij}\bar{y}_i l_{ik}, && (11)\\
-E[\frac{\partial^2 L}{\partial\lambda_j\partial\mu_k}] &= -\sum_{i,t} c_{ijt}l_{ik}e^{-\sum_\xi l_{i\xi}\mu_\xi}\\
&= -\sum_i c_{ij}l_{ik}e^{-\sum_\xi -l_{i\xi}\mu_\xi}. && (12)
\end{aligned}$$

Replacing $\Delta\theta$ with $[\Delta\lambda^T, \Delta\theta^T]^T$, (8) becomes

$$\begin{pmatrix} F_{\lambda\lambda} & F_{\lambda\mu} \\ F_{\lambda\mu}^T & F_{\mu\mu} \end{pmatrix} \begin{pmatrix} \Delta\lambda \\ \Delta\mu \end{pmatrix} = 0 \tag{13}$$

$F_{\lambda\lambda}$ is expected to be invertible, because the reconstruction of the activity is fairly stable when the attenuation is fixed. If $F_{\lambda\lambda}$ is indeed invertible, then $\Delta\lambda$ can be eliminated, yielding

$$(F\mu\mu - F_{\lambda\mu}^T F_{\lambda\lambda}^{-1} F_{\lambda\mu})\Delta\mu = 0. \tag{14}$$

In the following, we show that for non-TOF systems, and in particular near the center of uniform objects, the operators $F\mu\mu$, $F_{\lambda\mu}$ and $F_{\lambda\lambda}$ are all very similar, such that the equation is expected to be (almost) satisfied for many possible local changes $\Delta\mu$. That results in cross-talk, the corresponding $\Delta\lambda$ can be computed from (8). However, incorporation of TOF information changes the operator $F_{\lambda\lambda}$, such that (14) does no longer have solutions for local changes $\Delta\mu$.

Inserting (10)-(12) into (13) yields

$$\begin{aligned}
\sum_{kit} \frac{c_{ijt}c_{ikt}}{\bar{y}_{it}} e^{-2\sum_\xi l_{i\xi}\mu_\xi}\Delta\lambda_k &= \sum_{ki} c_{ij}l_{ik}e^{-\sum_\xi l_{i\xi}\mu_\xi}\Delta\mu_k\\
\sum_{ki} l_{ij}c_{ik}e^{-\sum_\xi l_{i\xi}\mu_\xi}\Delta\lambda_k &= \sum_{ki} \bar{y}_i l_{ij} l_{ik}\Delta\mu_k && (15)
\end{aligned}$$

For the non-TOF case, the TOF-index $t$ must be dropped, and the first equation in (15) becomes:

$$\sum_{ki} \frac{c_{ij}c_{ik}}{\bar{y}_i} e^{-2\sum_\xi l_{i\xi}\mu_\xi}\Delta\lambda_k = \sum_{ki} c_{ij}l_{ik}e^{-\sum_\xi l_{i\xi}\mu_\xi}\Delta\mu_k$$

The coefficients $c_{ij}$ and $l_{ij}$ both represent the contribution of pixel $j$ to the acquisition along LOR $i$ and should have very similar values. Assuming they are identical except for a factor (which can be absorbed in $\lambda$ or $\mu$ by changing the units), the non-TOF equations become:

$$\begin{aligned}
\sum_i l_{ij} \frac{e^{-\sum_\xi l_{i\xi}\mu_\xi}}{\bar{y}_i} \sum_k l_{ik}(e^{-\sum_\xi l_{i\xi}\mu_\xi}\Delta\lambda_k - \bar{y}_i\Delta\mu_k) &= 0\\
\sum_i l_{ij} \sum_k l_{ik}(e^{-\sum_\xi l_{i\xi}\mu_\xi}\Delta\lambda_k - \bar{y}_i\Delta\mu_k) &= 0 && (16)
\end{aligned}$$

An extreme case is obtained when the attenuation corrected counts $\bar{y}_i e^{\sum_\xi l_{i\xi}\mu_\xi}$ are constant for all LORs $i$ that intersect the region where $\Delta\lambda$ is non zero. In that case, the two sets of equations in (16) become identical and will have non-zero solutions. For example, if one considers a small change at a single pixel $k$, the solution equals

$$\frac{\Delta\lambda_k}{\Delta\mu_k} = \bar{y}_i e^{\sum_\xi l_{i\xi}\mu_\xi}. \tag{17}$$

The use of time-of-flight changes the elements of the submatrix $F_{\lambda\lambda}$ in the Fisher information matrix, destroying the similarity between the two equations. As a result, pixel-by-pixel cross-talk becomes impossible.

### C. *Uniqueness of the solution*

The analysis above indicates that TOF-information eliminates high frequency cross-talk between the emission and attenuation reconstructions in the joint estimation. However, it does not exclude low frequency cross-talk. In our experiments, we observed that MLAA produces images that are visually free of artifacts, but differ from the true images by a scale factor. Here we attempt to gain some insight in this scaling effect, by deriving a scaled solution from the true image. Assume that the true tracer distribution is $\lambda(\vec{x})$ and the true attenuation map is $\mu(\vec{x})$. The tomograph is centered at $\vec{x} = (0,0)$. We also assume that $\lambda(\vec{x}) = 0$ and $\mu(\vec{x}) = 0$ when $|\vec{x}| > R$. The sinogram attenuation factors due to the attenuation image $\mu$ equal $\exp(-P\mu) = m(s,\theta)$, where $s$ is the distance between the LOR and the center, $\theta$ is the projection angle and $P$ is the (non-TOF) projection operator. Consequently, the attenuated emission sinogram equals $y(s,t,\theta) = (P_t\lambda)(s,t,\theta)\ m(s,\theta)$, where $P_t$ is the TOF-projector and $t$ the TOF-index.

Now consider a non-TOF sinogram $n$ which is uniform within the boundary $B$ of the considered object: $n(s,\theta) = \ln(\alpha)$ with $\alpha > 0$ if $(s,\theta) \in B$ and $n(s,\theta)$ is allowed to have any values ouside $B$. Consistent sinograms satisfying the above condition can be found so there exists an image $\mu_\alpha$ such that inside $B$ we have $P\mu_\alpha = \ln(\alpha)$ and hence $\exp(-P\mu_\alpha) = 1/\alpha$. Thus, the attenuation created by the modified attenuation map $(\mu + \mu_\alpha)(\vec{x})$ equals $m(s,\theta)/\alpha$. It follows that the sinogram $y$ can be obtained with activity image $\alpha\lambda$ and attenuation map $\mu + \mu_\alpha$, for any $\alpha$ for which $\mu + \mu_\alpha \geq 0$. Note that with this construction, the activity is globally scaled, while the attenuation undergoes a position dependent scaling.

Furthermore, when the object boundary is known exactly and the attenuation values are set to zero outside the boundary, $n(s,\theta) = \ln(\alpha)$ if $(s,\theta) \in B$ and $n(s,\theta) = 0$ if $(s,\theta) \notin B$, the sinogram $n(s,\theta)$ is no longer consistent. This is due to the singularities in $\mu_\alpha$ present at the object boundaries which would make it unlikely for any joint estimation reconstruction to reach a scaled solution of the true images. This would imply that the solution of joint estimation is truly unique with a known object boundary. However, our first experiments indicate that the practical value is questionable, because small errors in the object boundary seem to be enough to reintroduce the scaling problem.

In [28], this problem is studied based on a consistency condition for 2D TOF-PET data. It was shown there that the set of scaled solutions $\{\alpha\lambda, \mu + \mu_\alpha : \alpha > 0\}$ described above are the only solutions to the joint estimation problem from TOF-PET emission data. Thus, it will still be necessary to use some a-priori knowledge about the expected intensities of the activity and/or the attenuation images. In most cases, the most convenient will be to use a priori values for the attenuation in tissue.

## III. EXPERIMENT DESIGN

### A. *2D Simulations*

Figure 1 shows the two phantoms used in our 2D phantom studies. Simulations of a $16 \times 16$ 2D circular phantom are used to study the features of the FIM for non-TOF and TOF PET systems. A 2D phantom of the thorax is used to study visual quality, bias and noise of MLAA reconstructions as a function of TOF resolution. We use a Field-Of-View (FOV) of 40 cm for the study of the features of the FIM and the study of visual quality of the reconstructions as a function of time resolution and iterations. For the study of bias and noise, more realistic TOF specifications adjusted to commercially available TOF-PET systems will be used. Furthermore, the activity images will be shown in a white-to-black color map whereas a black-to-white color map will be used to show the attenuation images.

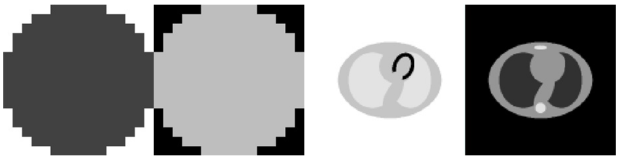

Fig. 1. Attenuation and activity images of the simulated phantoms: left: the 16x16 pixels phantom to study the Fisher information matrix, right: the 2D thorax phantom.

*1) The Fisher information matrix:* In this study, the $16 \times 16$ circular phantom shown in figure 1 with uniform activity and uniform tissue attenuation in the attenuation map was used. The field of view had a diameter of 40 cm and the pixel size was 2.5 cm. For this toy problem, the Fisher information matrix can be computed explicitly because its size is only $512 \times 512$. Non-TOF submatrices of the Fisher information matrix were compared to a TOF system with a spatial resolution of 2.5 cm FWHM. The submatrices $F_{\lambda\lambda}, F_{\lambda\mu}$ and $F_{\mu\mu}$ can be considered as operators, and their impulse response for the central pixel in the phantom was computed. As shown in eq (8), the size of the null space is determined by the rank of the Fisher information matrix. Therefore, its singular values and condition number were computed for non-TOF PET and for TOF-PET with different TOF resolutions.

*2) Thorax Phantom:* For the 2D thorax phantom, shown in fig 1, 2D sinograms with 128 detectors (bin size 3.125 mm), 128 projection angles over 180 degrees were computed and a TOF sampling density of at least 4/FWHM$_{\text{TOF}}$ were generated. An oversampling of 3 was used during simulation (i.e. 3 rays per LOR, 9 sub-pixels per image pixel). The reconstructed images had $128 \times 128$ pixels and because we study the stability, unpenalized MLAA was used. However, the emission data provide no attenuation information about LORs that do not intersect the activity distribution. To solve this, we produce an estimate of the object boundary by thresholding either the sinogram or the initial reconstruction, and apply an intensity prior that favors zero attenuation values outside that body contour. The prior was set to have a negative derivative in every voxel except for voxels with zero and tissue attenuation values.

The simulations were conducted for varying TOF resolutions, from 40 cm (approximately non-TOF) to 2.5 cm corresponding to time resolutions of 2667 ps to 167 ps. Simultaneous activity and attenuation images were reconstructed varying the number of iterations to study the convergence properties. For these experiments the attenuation image was initialized by filling the correct body contour uniformly with tissue attenuation and a uniform activity within the FOV was used as the initial activity image.

After the analysis of the influence of the TOF time resolution on the final reconstructions, the simulation specifications were adjusted according to the Siemens Biograph mCT scanner specifications for the study on initialization and noise. For the 2D thorax phantom shown in fig 1, 2D sinograms with 200 detectors (bin size 4.01 mm) and 168 projection angles over 180 degrees were generated. An effective TOF-resolution of 580 ps (= 8.7 cm) FWHM and a time-bin width of 312 ps were used to generate the sinograms. An oversampling of 3 was used during simulations, the reconstructed images had 200 × 200 pixels and as before unpenalized MLAA was used.

We studied the effect of different initializations on the final MLAA reconstructions. Attenuation maps with the correct body contour were filled with 0.5, 1 and 2 times tissue attenuation. Also a zero image, an image with random noise and an image designed to encourage cross-talk near the heart were used for this purpose.

Poisson noise was then added to the sinogram of the 2D thorax phantom to analyze the behaviour of MLAA under noisy conditions. The maximum count in the sinogram was chosen to be less than 10. The activity and attenuation maps were reconstructed from this noisy sinogram starting from uniform initial images. As reference images, we used the MLEM reconstruction of the activity using the true attenuation coefficients and the MLTR reconstruction of the attenuation using the true activity distribution. The same experiment was done for a noiseless sinogram. We assumed that the difference between the noisy and the noise-free reconstructions is due to noise in the emission measurements only. From these images, noise correlation coefficients were computed between the MLAA reconstructions and the reference reconstructions.

### *B. Phantom scans and patient study*

A fully 3D implementation of MLAA has been applied to two scans of a phantom and to a clinical patient study. The scans have been acquired on a Siemens Biograph mCT system. The TOF-PET data are organized as 5D sinograms, consisting of 400 radial bins, 168 azimuthal angles, 9 co-polar angles, up to 109 planes (depending on the co-polar angle) [29], and 13 time bins of 312 ps width, with an effective TOF resolution of 580 ps.

By simple thresholding and backprojection operations, a reasonable estimate of the body contour can be obtained [7]. In order to deal with the scale problem in the MLAA reconstructions, we impose the known value of tissue attenuation to the 75th percentile of the attenuation value within this (initial) body contour. This value is imposed by scaling the entire attenuation image. For the images considered here, the 75th percentile corresponded to tissue, but of course, more sophisticated segmentation algorithms could be used for this purpose.

Outside this region however, a background prior was used to encourage background attenuation values to become zero. In both 3D studies, the smoothing relative difference prior of [30] was also used to encourage smoothness in the attenuation map.

*1) 3D Phantom Study:* The NEMA IEC body phantom [31] was used to evaluate the simultaneous activity and attenuation reconstructions in 3D. The measurements corresponded to a 5 minute scans of 6.18 mCi injection scanned 2 hours post-injection. The phantom was located once in the center of the FOV and once closer towards the edge of the FOV. The reconstructed activity and attenuation images were analyzed in two studies. In the first study, the contributions of scatter were not taken into account and we did not try to enforce bed attenuation in the attenuation image. However in the second 3D phantom study, the CT-based scatter estimate and bed attenuation values were used during MLAA reconstructions.

*2) Clinical study:* A clinical five minute scan of the thorax of a patient injected with 570 MBq $^{18}$F-FDG was used to reconstruct the activity and attenuation images. The TOF-PET measurements suffer from truncation near the edge of the FOV of the system. As shown below, the truncation affected the reconstruction of the arms in the PET and CT images, as well as in the MLAA images. In order to reduce the effects of scatter and attenuation values outside the support of the patient, we used the precomputed CT scatter estimate and imposed the CT-based bed attenuation in the attenuation image.

## IV. RESULTS

### *A. 2D Simulations*

*1) Nullspace of the FIM:* The four elements of the FIM defined in equation 9 are computed for the 16 × 16 circular phantom of figure 1 for both a NON-TOF and a TOF system. Since only the first term of the FIM incorporates both TOF-projection and TOF-backprojection operators, the elements of the first quadrant of the FIM, $F_{\lambda\lambda}$ , change for a TOF system while the other three parts remain unchanged. Figure 2 shows the central row of each matrix reshaped into the size of the emission and attenuation images. It is good to know that this row also corresponds to the voxel located near the center of the FOV.

The top row of figure 2 shows the FIM response in the emission image for a small change of the activity in the voxel located close to the center of the FOV, for both TOF and non-TOF. The left figure in the bottom row of figure 2 shows the influence of a small change in the attenuation seen in the emission image and vice versa. The right figure shows the effect of a change in the attenuation image for a change of the attenuation for the same voxel located near the center of the FOV. Using the term Point Spread Function (PSF) with caution[1], figure 2 shows the four PSFs of the central voxel in the FOV of the system in the Fisher information matrix.

[1] position dependant PSF in the FIM

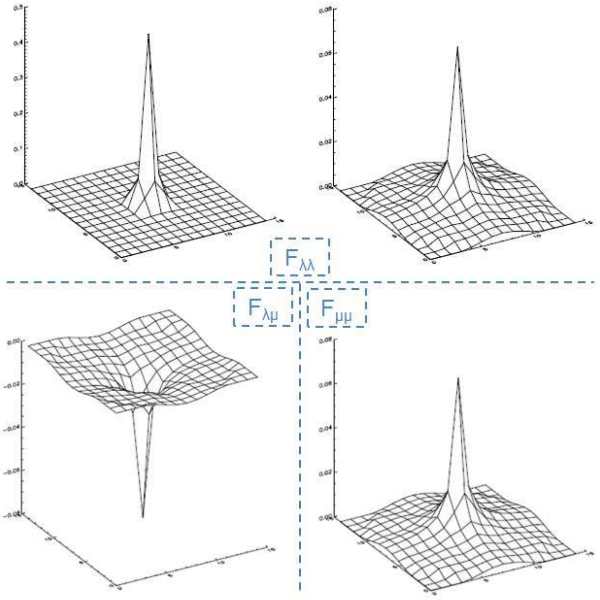

Fig. 2. The four Fisher Information PSFs for a change located near the center of the FOV. Top: the effect of a change of emission parameters into the emission image for a TOF and a NON-TOF system, bottom-left: the effect of a change in the emission data seen in the attenuation image and vice versa, Bottom-right: the effect of a change of attenuation seen in the attenuation image.

It can be seen from figure 2 that for a non-TOF system and for some simultaneous change in the emission and attenuation values of the voxel located near the center of the FOV, these changes can potentially cancel each other out (as long as they don't violate the positivity constraint). Hence, these changes can not be identified from the measurements because they do not modify the value of the likelihood, which remains at its maximum. On the other hand, for a TOF system the four PSFs are no longer similar. Thus, any change in the activity or attenuation values of the same voxel can be fully described by itself and not by the other, which makes activity and attenuation cross-talk impossible.

According to the rank-nullity theorem and based on the facts discussed above, the rank of the FIM would be close to $J$ for a non-TOF system, while it would be much higher for a TOF system. We used Singular Value Decomposition (SVD) as a rank revealing decomposition to investigate this. Figure 3 shows the singular values computed for the Fisher information matrix for a non-TOF system and multiple TOF systems with different time resolutions plotted on a logarithmic scale. It can be seen that the singular values of the FIM grow as the time resolution of a TOF system increases, hence, the Fisher information matrix becomes better-conditioned.

*2) Thorax Phantom:* Figure 4 shows the resulting activity and attenuation reconstructions of the noiseless thorax phantom after 5, 15 and 50 iterations of MLAA for varying TOF-resolutions. In this study, in order to have a better understanding of MLAA convergence, the attenuation images were updated only once for each update of the activity.

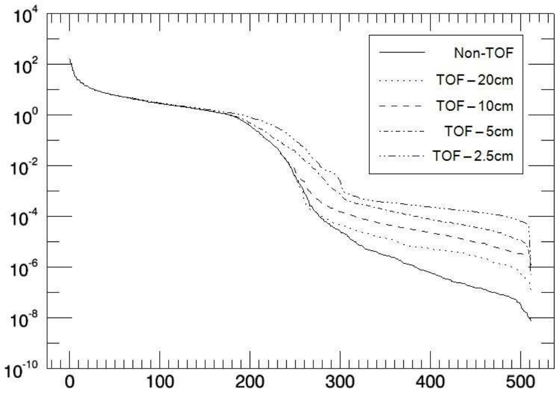

Fig. 3. Singular values computed for the FIM for a non-TOF system and multiple TOF systems with time resolutions varying from 20cm to 2.5cm FWHM.

It can be seen from figure 4 that, after 50 iterations of MLAA the estimated activity and attenuation maps for a TOF resolution of 40 cm FWHM still suffer from cross-talk and do not visually converge to the true images. Improving the time resolution to 20 cm FWHM, the reconstructions after 50 iterations improve significantly, however they still differ from the true images. For TOF resolutions below 20cm FWHM the reconstructions visually converge to the true image. However, the reconstructions differ from the true images by a scaling factor which can not be seen here. It can also be seen that as the TOF resolution increases the speed of convergence increases as well.

To study the effect of initialization on joint activity and attenuation estimation, we initialized MLAA with various initial images which all visually converged to very similar images. We also used a non-TOF reconstructed image of the thorax phantom, which suffered greatly from activity and attenuation cross-talk, to initialize a TOF-MLAA reconstruction. Figure 5 shows the initial images suffering from cross-talk and the final activity and attenuation reconstructions. As with all the other initial images used, after sufficient iterations of the algorithm, the reconstructions visually converged to the true image, but they differed by a scale factor.

Figure 6 compares the MLAA reconstructions from a noisy

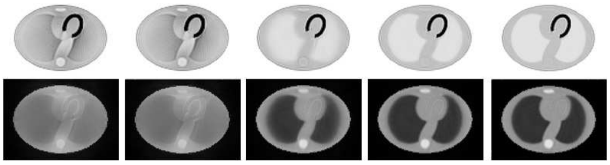

a) After 5 iterations

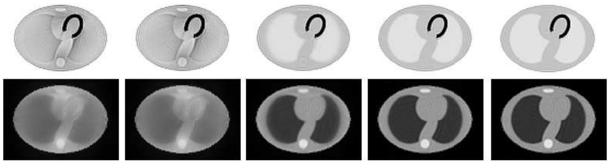

b) After 15 iterations

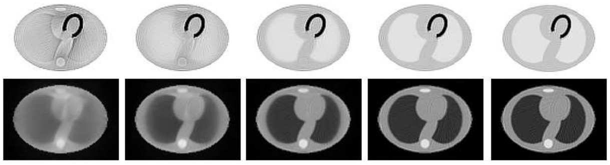

c) After 50 iterations

Fig. 4. Activity and attenuation reconstructions after 5, 15 and 50 iterations and 32 subsets of MLAA for TOF resolutions of 40 cm (approximately non-TOF), 20 cm, 10 cm, 5 cm and 2.5 cm.

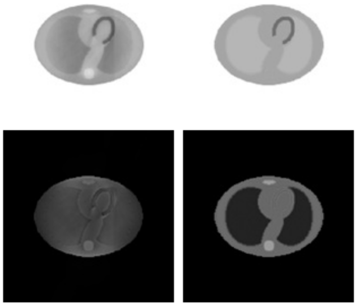

Fig. 5. Activity (top) and attenuation (bottom) images reconstructed from non-TOF reconstructions used as initial images (left) suffering highly from cross-talk and the final TOF-MLAA reconstructions (right).

sinogram to the reference images computed from MLEM and MLTR reconstructions, where a strong noise correlation is visible. A noise correlation coefficients of 0.86 was computed for the MLAA reconstructed activity image starting from uniform initial images with respect to the MLEM reconstructed activity image with a known attenuation map. The same measure was computed to be 0.98 for the MLAA reconstructed attenuation map with respect to the MLTR reconstructed attenuation map with a known activity image. This high noise correlation suggests that TOF simultaneous reconstruction handles noise just as reconstructions from known activity or attenuation maps. Apparently, the noise in the sinogram does not propagate to make simultaneous reconstructions unstable.

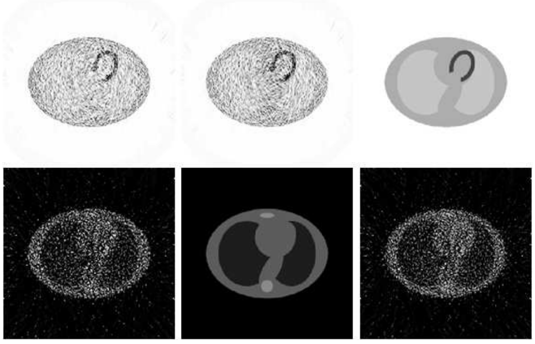

Fig. 6. Activity (top) and attenuation (bottom) images reconstructed from a noisy sinogram. The reconstructed results of MLAA initialized by uniform images (left) are compared to that of an MLEM (center) and MLTR (right) with known attenuation and activity maps respectively.

### *B. Phantom scans and patient study*

*1) 3D Phantom study:* Results from 3D reconstructions of activity and attenuation of the NEMA IEC body phantom located near the FOV center of the mCT are shown in figures 7 and 8. The resulting reconstructions are shown for two different transversal planes: one having more details in the activity image, figure 7, and one with more details in the attenuation image, figure 8. The MLAA reconstructions are compared to the CT-based attenuation image and the OSEM reconstructions of the activity with CT-based attenuation correction. The reconstructions shown here are from 3 MLAA iterations of 42 subsets.

The TOF-MLAA reconstructions do not suffer from activity and attenuation cross-talk. However, because we did not correct for scatter, there is slight activity present within the cavity of the NEMA phantom and some excess attenuation around the object of interest. This could be expected for reconstructions that do not compensate for scatter. It can also be seen in figure 8 that the algorithm has tried to compensate for bed attenuation by putting attenuation values outside the support of the object. Using the CT-based scatter estimate and bed attenuation during MLAA reconstructions, activity and attenuation images were reconstructed free of these artifacts, however, the results are not shown here. Similar results were also obtained for the phantom in the off-center position.

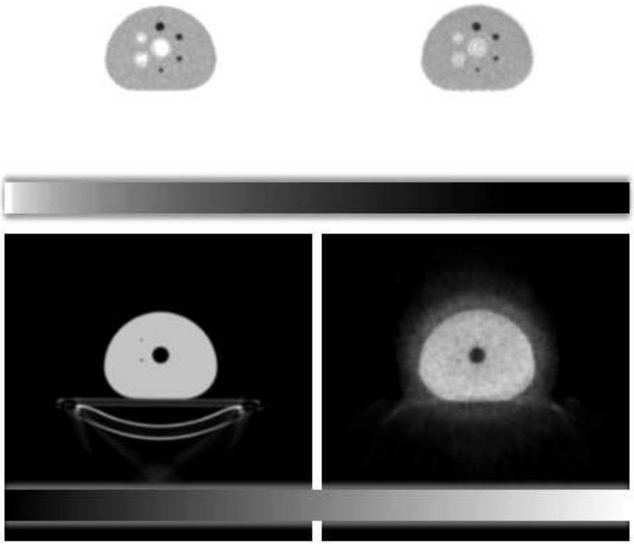

Fig. 7. CT attenuation corrected MLEM reconstructions (top-left), FBP attenuation reconstruction of the CT (bottom-left), MLAA reconstructed emission (top-right) and attenuation (bottom-right) images of the 3D NEMA phantom located near the center of the FOV.

*2) Clinical Study:* Figures 9 and 10 show the activity and attenuation reconstructions from the clinical data, respectively. The activity reconstructed from OSEM with CT-based attenuation correction and the one of MLAA are shown in figure 9 and the CT attenuation image and the reconstructed MLAA attenuation image are shown in figure 10. The two activity reconstructions shown in 9 look visually very similar but a quantitative analysis should be done to verify the degree of similarity of the two reconstructions.

Looking at the attenuation reconstruction of MLAA in figure 10, a good lung-tissue discrimination is observed. The algorithm has also been able to produce a fairly good estimate of the patient body contour making use of the tracer uptake in the entire body. However, the attenuation values are slightly elevated near the heart. This is probably due to significantly higher activity uptake in the heart, but further analysis is needed.

Comparison of the two attenuation reconstructions of the CT and MLAA, figure 10, shows that the MLAA attenuation reconstructions suffer less from truncation artifacts. This is partly because the CT scanner uses a slightly smaller FOV compared to the PET scanner of the mCT, and because iterative algorithms handle truncation better than analytic reconstructions. In this comparison, the portion of the liver

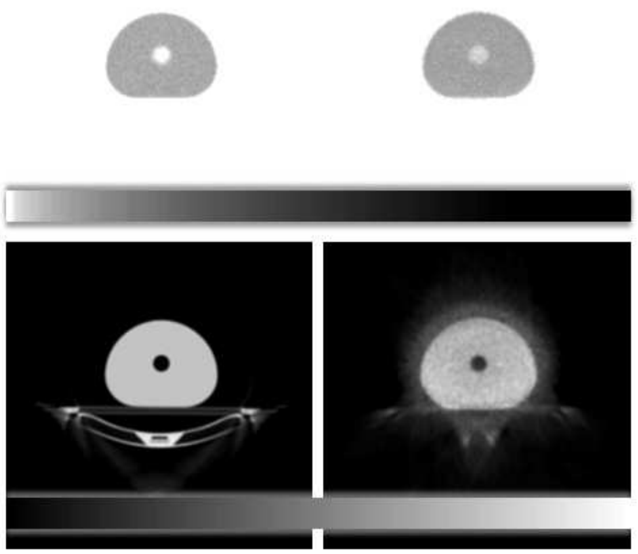

Fig. 8. CT attenuation corrected MLEM reconstructions (top-left), FBP attenuation reconstruction of the CT (bottom-left), MLAA reconstructed emission (top-right) and attenuation (bottom-right) images of the 3D NEMA phantom located near the center of the FOV.

visible in the lung of the patient is slightly different, which is due to the breathing motion during acquisition.

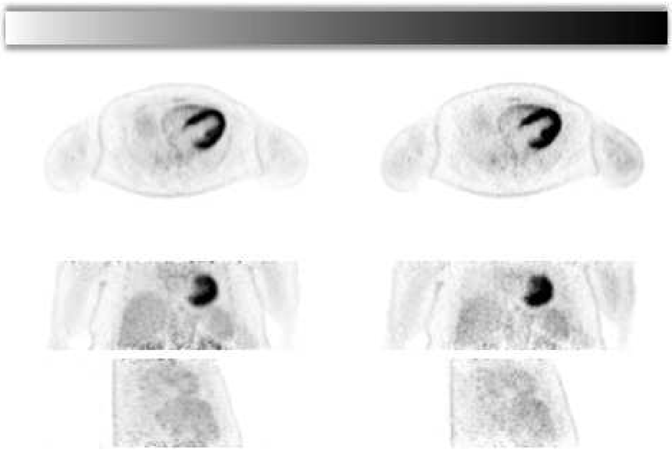

Fig. 9. Transverse (top), coronal (center) and sagittal (bottom) view of the activity corrected with CT-based attenuation (left) and the activity reconstructed with MLAA (right). The MLAA image was smoothed with a 3D Gaussian with 6 mm FWHM to match approximately the resolution of the standard reconstruction. The horizontal bar represents the gray level lookup table.

## V. DISCUSSION

Simultaneous reconstruction of attenuation and activity in SPECT and non-TOF PET has been investigated by many groups, and was found to be a very ill-posed problem. Previous studies have shown that the use of Time-of-Flight reduces the sensitivity of the PET reconstruction to attenuation correction errors. The study presented here reveals that Time-of-Flight information has the ability to stabilize the joint estimation problem, and may therefore enable quantitative PET imaging without relying on transmission scans or other anatomical imaging procedures. Estimating the attenuation from the emission data has the advantage that it ensures a correct match with respect to photon energy and patient position, and probably a good match in the presence of motion blurring (e.g. heart beat, breathing).

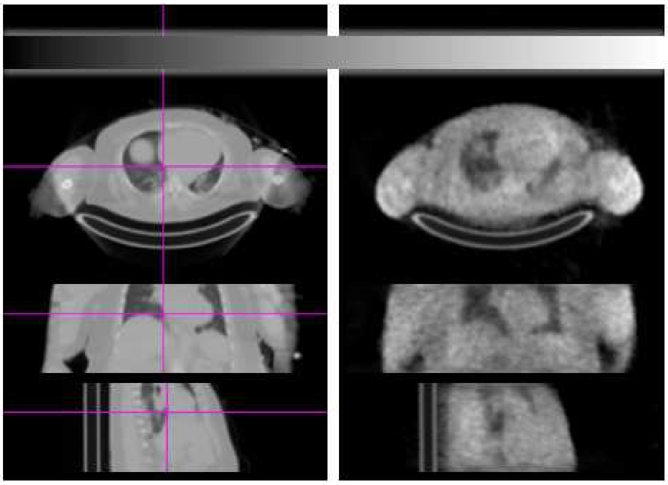

Fig. 10. Transverse (top), coronal (center) and sagittal (bottom) view of the CT-based attenuation image (left) and attenuation image reconstructed with MLAA from the emission data (right). The MLAA image was smoothed with a 3D Gaussian with 6 mm FWHM. The horizontal bar represents the gray level lookup table.

As suggested by our experiments, and as proven by the theoretical analysis in [28], the TOF-PET data enable the estimation of the attenuation sinogram up to a constant term, and therefore the estimation of the activity up to a constant factor. It is anticipated that in most applications, this constant can be determined in a fairly straightforward way by imposing the known attenuation value of tissue to a segmented portion of the attenuation map. An alternative way would be to combine the method with full or partial transmission information, which could e.g. be obtained by adding transmission source(s) in the field of view [32].

The PET emission data provide no (or at least incomplete) information about attenuation along LORs that do not intersect a region containing a significant amount of radioactive tracer. Many tracers, including $^{18}$F-FDG, show uptake in the entire body. For such tracers, it is valid to assume that the attenuation along LORs without activity is zero everywhere. In our experiments, we have applied a prior encouraging the assignment of zero attenuation to such regions. The PET emission data are also noisy. In our experiments, the regularization was restricted to the use of a smoothing Markov prior in the attenuation image, and a small amount of post-smoothing of the activity image. Many other priors have been proposed for emission and transmission tomography. Evaluation of such priors for regularization of this joint estimation problem is a topic for further research.

Reconstructions of the activity and attenuation maps with an effective smoothing and background prior and without the addition of the bed to the attenuation map could lead to slight over-estimation of the true support of the attenuation map in order to compensate for bed attenuation. It should also be noted that the attenuation reconstructions outside the activity region have a slower convergence rate than the portion of the attenuation map inside the region. For these reasons, adding the effect of additional attenuating medium, specifically the bed, to the attenuation reconstruction instead of reconstructing the bed along with the unknown attenuation medium would be a more reasonable and practical approach.

We initialized a TOF-MLAA reconstruction with images that suffered from cross-talk. The final reconstructions did not show signs of cross-talk which indicates that TOF-MLAA is able to get rid of any cross-talk already present in the initial images. This is a good thing since we un-intentially introduce some cross-talk in the initialization step where we keep the initial attenuation image fixed for a long time to find an initial image to use for the activity image.

In the NEMA IEC phantom study, we did not compensate for any scatter in the measurements and still were able to achieve reasonable reconstructions. This goes to show that fairly good reconstructions could be made without any scatter compensation. We believe that given these scatter un-compensated reconstructions, it is possible to make an estimate of the scatter and refine the final activity and attenuation reconstructions in an additional step.

In the clinical patient study, the patient was injected with a non-specific tracer that has a detectable accumulation in all tissues, which made the attenuation reconstruction with roughly the true support possible. For more specific tracers that do not dissipate to the entire body, reconstruction of the attenuation map with the correct support might prove to be more difficult. The use of an external source could help in these situations.

## VI. Conclusion

In this paper, the feasibility of simultaneous activity and attenuation reconstruction from the measurement data was investigated for a Time-of-Flight system. The existing MLAA algorithm which makes alternated updates to the activity and attenuation maps by means of the existing MLEM and MLTR algorithms was used for this purpose.

The feasibility of this approach was verified for 2D and 3D phantom studies as well as for a clinical study. It was found that the utilization of Time-of-Flight information in simultaneous reconstructions eliminates the problem of activity and attenuation cross-talk. However, since the problem of joint estimation is still ill-posed, limited prior knowledge is required.

It was shown that as the time resolution of the TOF system increases, the convergence towards the true images increases as well. The joint ML reconstruction was found to be robust to noise in the emission sinogram.

## References

[1] Kinahan P E, Townsend D W, Beyer T, Sashin D. "Attenuation correction for a combined 3D PET/CT scanner". *Med Phys* 1998; 25 (10): 2046-2053

[2] H Zaidi, B H Hasegawa, "Attenuation correction strategies in Emission Tomography" in *Qualitative analysis in nuclear medicine imaging*, H Zaidi, Springer Science + Business Media Inc. 2006

[3] M Defrise, P E Kinahan, C J Michel, "Image Reconstruction algorithms in PET" in *Positron Emission Tomography*, D L Bailey, D W Townsend, P E Valk, M N Maisey Springer-Verlag London Limited 2005

[4] Y Censor, DE Gustafson, A Lent, and H Tuy, "A new approach to the emission computerized tomography problem: simultaneous calculation of attenuation and activity coefficients," *IEEE Trans Nucl Sci*, vol. NS-26, pp. 2775–2279, 1979.

[5] F Natterer,"Determination of tissue attenuation in emission tomography of optically dense media," *Inverse Problems*, vol. 9, pp. 731–736, 1993.

[6] A Welch, R Clack, F Natterer et al., "Toward accurate attenuation correction in SPECT without transmission measurements", *IEEE Trans Med Imaging*, 1997, 5:532-541.

[7] J Nuyts, P Dupont, S Stroobants, R Benninck, L Mortelmans, P Suetens, "Simultaneous maximum a-posteriori reconstruction of attenuation and activity distributions from emission sinograms", *IEEE Trans Med Imaging*, 1999, 18:393-403.

[8] A V Bronnikov, "Reconstruction of attenuation map using discrete consistency conditions", *IEEE Trans Med Imaging*, 2000, 19:451-462.

[9] Kudo H and Nakamura H, "A new approach to SPECT attenuation correction without transmission measurements," *Nuclear Science Symposium and Medical Imaging Conference*, pp. 13–59 – 13–62, 2000.

[10] V Y Panin, G L Zeng, G T Gullberg "A method of attenuation map and emission activity reconstruction from emission data", *IEEE Trans Nuc. Science*, 2001, 48:131-138.

[11] A Krol, JE Bowsher, SH Manglos et al., "An EM algorithm for estimating SPECT emission and transmission parameters from emission data only", *IEEE Trans Med Imaging*, 2001, 20:218-232.

[12] De Pierro A, Crepaldi F. "Activity and attenuation recovery from activity data only in emission computed tomography". *Comput Appl Math* 2006: 25: 2-3.

[13] CM Laymon and JE Bowsher, "A log likelihood based method for recovery of localized defects in PET attenuation-correction images," *IEEE Nucl Sci Symp Conf Record*, pp. 2710–2714, October 2004.

[14] J Nuyts, C Michel, M Fenchel et al., "Completion of a truncated attenuation image from the attenuated emission data"., *IEEE Nucl Sci Symp Conf Record* Knoxville, TN, USA, oct-nov 2010.

[15] A Salomon, A Goedicke, B Schweizer et al., "Simultaneous reconstruction of activity and attenuation for PET/MR", *IEEE Trans Med Imaging*, 2011, 30:804-813

[16] W W Moses, "Time of Flight in PET revisited", *IEEE Trans Med Imaging*, 2003, 50:1325-1330

[17] M Conti, B Bendriem, M Casey et al., "First experimental results of time-of-flight reconstruction on an LSO PET scanner", *Phys Med Biol* 2005, 50:4507-4526.

[18] S Surti, A Kuhn, M E Werner et al., "Performance of Philips Gemini TF PET/CT scanner with special consideration for its time of flight imaging capabilities" *J Nucl Med* 2007, 48:471-480.

[19] B W Jakoby, Y Bercier, M Conti et al., "Physical and clinical performance of the mCT time-of-flight PET/CT scanner" *Phys Med Biol* 2011, 56:2375-2389.

[20] M Conti. "Why is TOF PET reconstruction a more robust method in the presence of inconsistent data?", *Phys Med Biol* 2011, 56:155-168.

[21] W Wang, Z Hu, E E Gualtieri et al., "Systematic and distributed Time-of-Flight List mode PET reconstructions", *IEEE Nucl Sci Symp Conf Record* San Diego, CA, USA, oct-nov 2006.

[22] K Vunckx, L Zhou, S Matej et al., "Fisher Information-based Evaluation of Image quality for Time-of-Flight PET", *IEEE Trans Med Imaging*, 2010, 29:311-321

[23] LS Shepp, Y Vardi. "Maximum likelihood reconstruction for emission tomography", *IEEE Trans Med Imaging*, vol MI-1, pp. 113-122, 1982.

[24] JA Fessler, EP Ficaro, NH Clinthorne, K Lange. "Grouped-Coordinate Ascent Algorithms for Penalized-Likelihood Transmission Image Reconstruction", *IEEE Trans Med Imaging* 1997; 16: 166-175.

[25] J Nuyts, B De Man, P Dupont, M Defrise, P Suetens, L Mortelmans."Iterative reconstruction for helical CT: a simulation study" *Phys Med Biol*, 1998; 43: 729-737.

[26] J A Fessler, W L Rogers, "Spatial resolution properties of Penalized-likelihood image reconstruction: Space-Invariant Tomographs", *IEEE Trans Med Imaging*, 1996, 5:1346-1358

[27] Q Li, E Asma, J Qi, J R Bading, R M Leahy "Accurate estimation of the fisher information matrix for the pet image reconstruction problem", *IEEE Trans Med Imaging*, 2004, 23:1057-1064

[28] M Defrise, A Rezaei, J Nuyts, "Time-of-flight PET data determine the attenuation sinogram up to a constant" submitted to *Phys Med Biol*

[29] F H Fahey, "Data aquisition in PET imaging", *J Nucl. Med. Technol*, 2002, 30:39-49.

[30] J Nuyts, D Beque, P Dupont et al., "A Concave prior penalizing relative differences for maximum-a-posteriori reconstruction in emission tomography", *IEEE Trans Nuc. Science*, 2002, 49:56-60.

[31] "www.spect.com/pub/NEMA_IEC_Body_Phantom_Set.pdf",

[32] P Mollet, K Keereman, S Vandenberghe, "Experimental evaluation of simultaneous emission and transmission imaging using TOF information" *Nuclear Science Symposium and Medical Imaging Conference*, Valencia, Spain, Oct 2011.